The Astrophysical Journal Letters, 924:L11 (6pp), 2022 January 1 https://doi.org/10.3847/2041-8213/ac441f

Stochastic Low-frequency Variability in Three-dimensional Radiation Hydrodynamical Models of Massive Star Envelopes

William C. Schultz[1], Lars Bildsten[1,2], and Yan-Fei Jiang (姜燕飞)[3]
[1] Department of Physics, University of California, Santa Barbara, CA 93106, USA
[2] Kavli Institute for Theoretical Physics, University of California, Santa Barbara, CA 93106, USA
[3] Center for Computational Astrophysics, Flatiron Institute, New York, NY 10010, USA

Received 2021 October 26; revised 2021 December 13; accepted 2021 December 17; published 2022 January 6

Abstract

Increasing main-sequence stellar luminosity with stellar mass leads to the eventual dominance of radiation pressure in stellar-envelope hydrostatic balance. As the luminosity approaches the Eddington limit, additional instabilities (beyond conventional convection) can occur. These instabilities readily manifest in the outer envelopes of OB stars, where the opacity increase associated with iron yields density and gas-pressure inversions in 1D models. Additionally, recent photometric surveys (e.g., TESS) have detected excess broadband low-frequency variability in power spectra of OB star lightcurves, called stochastic low-frequency variability (SLFV). This motivates our novel 3D Athena++ radiation hydrodynamical (RHD) simulations of two 35 $M_\odot$ star envelopes (the outer ≈15% of the stellar radial extent), one on the zero-age main sequence and the other in the middle of the main sequence. Both models exhibit turbulent motion far above and below the conventional iron-opacity peak convection zone (FeCZ), obliterating any "quiet" part of the near-surface region and leading to velocities at the photosphere of 10–100 km s^{-1}, directly agreeing with spectroscopic data. Surface turbulence also produces SLFV in model lightcurves with amplitudes and power-law slopes that are strikingly similar to those of observed stars. The characteristic frequencies associated with SLFV in our models are comparable to the thermal time in the FeCZ (≈3–7 day^{-1}). These ab initio simulations are directly validated by observations and, though more models are needed, we remain optimistic that 3D RHD models of main-sequence O-star envelopes exhibit SLFV originating from the FeCZ.

Unified Astronomy Thesaurus concepts: Stellar physics (1621); Stellar phenomena (1619); Stellar dynamics (1596); Stellar processes (1623); Stellar convection envelopes (299); Stellar convective zones (301); Hydrodynamical simulations (767); Stellar structures (1631)

1. Introduction

The outer envelopes of OB stars present some of the most challenging environments for the current treatment of stellar convection. For stars with $M \gtrsim 25\,M_\odot$, the opacity (κ) increase associated with iron at $T \approx 180{,}000$ K causes the luminosity (L) to surpass the Eddington value, $L_{\rm Edd} = 4\pi GMc/\kappa$, which yields density and gas-pressure inversions in 1D stellar models (Joss et al. 1973; Paxton et al. 2013) and a vigorous 3D instability at an optical depth, $\tau_{\rm Fe}$. The instability stymies 1D models when the iron-opacity peak is located sufficiently close to the surface to develop significant turbulence.

Convective efficiency associated with the turbulence can be quantified by the parameter $\gamma \sim P_{\rm th} v_{\rm c} \tau / P_{\rm rad} c$, where $v_{\rm c}$ is the convective velocity, c is the speed of light, and the total thermal pressure, $P_{\rm th} = P_{\rm g} + P_{\rm rad}$, where $P_{\rm g}$ and $P_{\rm rad}$ are the gas and radiation pressure (Cox & Giuli 1968). This is essentially comparing convective transport to radiative diffusion. When $\gamma < 1$, substantial radiation losses occur in moving fluid elements, defining a critical optical depth $\tau_{\rm crit} \sim cP_{\rm rad}/v_{\rm c}P_{\rm th}$. In massive stars, $\tau_{\rm crit} \gtrsim 1000$, yielding large regions of these stellar envelopes susceptible to inefficient convection which has only recently been achieved in full 3D radiation hydrodynamical (RHD) simulations (Jiang et al. 2015, 2018). Additionally, the turbulent convection in the iron-opacity peak convection zone (FeCZ) likely plays a dynamical role, exciting plumes that may reach the surface and cause the long-observed microturbulence measured in spectral lines of these stars (Cantiello et al. 2009). Such a mechanism may well be playing a role, but 3D calculations of this regime (Jiang et al. 2015, 2017, 2018) found even more surprising properties of these massive star envelopes. For example, the 3D calculations revealed that the velocity and density fluctuations from the FeCZ propagate well out to the stellar photosphere (Jiang et al. 2015, 2018), eliminating the intervening radiative layer predicted in 1D models. These simulations also revealed the first understanding of the complex interplay of convective and radiative transport and how it depends on the ratio $\tau_{\rm Fe}/\tau_{\rm crit}$. Even further out in the envelope, helium recombination causes an even larger increase in opacity that can lead to continuum-driven winds, possibly impacting our understanding of luminous blue variable eruptions (Jiang et al. 2018).

This complex interplay of convection and radiation is now being probed by photometric observations of these stars from space-based telescopes (e.g., TESS; Ricker et al. 2015) which have detected ubiquitous low-amplitude temporal brightness variability. Regardless of their spectral class, metallicity (Z), or rotation rate, all massive stars exhibit broadband photometric variability up to 5 mmag (≈0.5%) on timescales of hours to days (Bowman et al. 2019a, 2019b, 2020; Bowman 2020), which is referred to as stochastic low-frequency variability (SLFV). These same stars also exhibit large-scale surface-velocity fluctuations with macroturbulence velocities of

10–120 $\mathrm{km\,s^{-1}}$ that are detected with ground-based, high-resolution spectroscopy (Simón-Díaz et al. 2017).

The origin of SLFV and large-scale velocity fluctuations is debated. One possible cause is internal gravity waves (IGWs) generated in the convective hydrogen-burning cores that propagate through the radiative envelope and manifest near the stellar surface (Aerts et al. 2009; Aerts & Rogers 2015; Lecoanet et al. 2019). However, their observability depends on the efficiency of both the excitation processes in the core and the propagation through the envelope. Significant theoretical (Goldreich & Kumar 1990; Lecoanet & Quataert 2013) and computational (Aerts et al. 2009; Aerts & Rogers 2015; Couston et al. 2018) investigations of this phenomenon have occurred. Inhomogeneities from stellar winds combined with rotational effects have also been proposed as a possible explanation for SLFV (Moffat et al. 2008; David-Uraz et al. 2017; Simón-Díaz et al. 2018) and hydrodynamical simulations are currently predicting SLFV signatures arising from line-driven wind instabilities (Krtička & Feldmeier 2018, 2021). A third possible cause is surface disturbances produced by the FeCZ (Cantiello et al. 2009; Jiang et al. 2015; Cantiello & Braithwaite 2019; Lecoanet et al. 2019), which we explore here with 3D RHD models of surface convection regions.

2. 3D Models

This work presents two new 3D RHD models: T42L5.0, a zero-age main-sequence (ZAMS) 35 $M_\odot$ star, and T35L5.2, a 35 $M_\odot$ star halfway through the main sequence. The model names reflect the effective temperatures, $T_{\rm eff}/10^4$ K, and luminosities, $\log(L/L_\odot)$.

2.1. Computational Methods

These 3D RHD simulations model massive star envelopes with the code `Athena++` (Stone et al. 2020) in spherical polar coordinates. The code solves the ideal hydrodynamic equations coupled with the time-dependent, frequency-integrated radiation transport equation for specific intensities over 100 discrete angles based on the numerical algorithm described in Jiang (2021). We use (128×128) to cover $(\theta, \phi) \in [0.4898\pi, 0.5102\pi] \times [0, 0.064]$ for model T42L5.0 and (256×256) to cover $(\theta, \phi) \in [0.4444\pi, 0.5556\pi] \times [0, 0.3491]$ for T35L5.2. Model T42L5.0 utilized 384 logarithmically spaced radial bins to span 6.8 $R_\odot$ to 8.2 $R_\odot$, while T35L5.2 covers 9.7 $R_\odot$ to 15.3 $R_\odot$ with 336 logarithmically spaced radial bins. Both simulations use periodic boundary conditions in the angular directions and open boundary conditions at the top of the boxes. At their bases, several ghost zones enforce fixed T, ρ, $F_{\rm r}$ and maintain $v_{\rm r} = 0$ (see Jiang et al. 2018). These simulations take 3000 Skylake cores 4 days to run 1 day of model time. The gravitational potential is taken to be spherically symmetric, $\phi(r) = -GM/r$, where G is the gravitational constant, r is the radial coordinate, and M is the total mass inside r. All the models were run with solar metallicity. We calculate opacities using OPAL opacity tables (Iglesias & Rogers 1996) and local densities and temperatures. These opacity tables do not include additional line forces in optically thin regions. Due to computational limitations and the long time required for heat to escape the base of the envelope (>100 days of model time), T42L5.0 and T35L5.2 reached thermal equilibrium down to $r = 7.1\,R_\odot$ and $r = 11.1\,R_\odot$, respectively, and both models' FeCZ evolved for nearly 100 thermal times. The analysis we present in this work only concerns the surface regions of the simulations, in which all properties of interest in the model (e.g., velocities, densities, temperatures) are in thermal equilibrium.

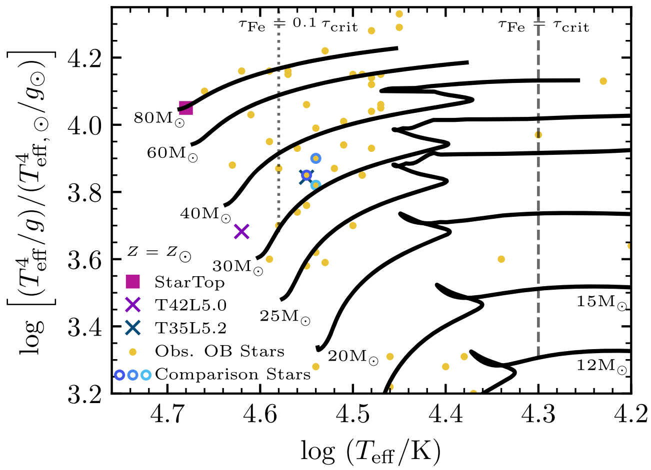

Figure 1. Spectroscopic HR diagram showing locations of new models (the two Xs) relative to recent TESS observations and stellar evolution tracks (the black lines). The gold circles denote OB star observations from Burssens et al. (2020) while the blue outlines surround stars against which our models are compared in Section 3. The magenta square symbolizes the StarTop model from Jiang et al. (2015): a plane-parallel model of the surface of an 80 $M_\odot$ star. The vertical lines denote locations where the optical depth to the iron-opacity peak, $\tau_{\rm Fe}$, is equal to (dashed) or 10% of (dotted) of $\tau_{\rm crit}$.

To perform a basic resolution study, we ran two additional models with the same initial conditions as T35L5.2: one with half the resolution and only 80 angles used for radiation as well as another with the same cell size but half the angular domain ((128×128) to cover $(\theta, \phi) \in [0.4898\pi, 0.5102\pi] \times [0, 0.064]$) and a smaller radial domain, spanning 10.9 $R_\odot$ to 15.3 $R_\odot$. We compare T35L5.3 to the lower resolution models in Section 3.

In this work, all 1D comparisons are with reference to Modules for Experiments in Stellar Astrophysics (MESA, Paxton et al. 2011, 2013, 2015, 2018, 2019) models. Specifically, MESA models generated using the default inlist values from version 15140 were used to both determine the stellar parameters to use as well as the initial conditions for the `Athena++` simulations. MESA models from Cantiello et al. (2021) were used to show stellar evolutionary tracks in Figure 1.

2.2. Model Parameters and Characteristics

Figure 1 shows where our 3D models lie in the spectroscopic HR diagram (sHRD) and compares them to previous RHD models, MESA stellar evolution tracks, and recent TESS observations of solar metallicity stars. T35L5.2 was chosen to closely match three TESS observations and T42L5.0 was chosen to be a more convectively quiet model for comparison and to probe dynamics in hotter stars with $\tau_{\rm crit} \ll \tau_{\rm Fe}$.

The stark contrast in variance of fundamental variables is depicted in Figure 2, which shows the variations in quantities of interest for single temporal snapshots of both models long after they have reached equilibrium. T42L5.0 shows nearly no variations throughout the optically thick region. This is likely because the entire profile of this model is sub-Eddington and convective flux carries <1% of the total flux.

In contrast, T35L5.2 displays significant variations at each radius including several orders of magnitude of density fluctuations in the optically thick region. Vigorous convection

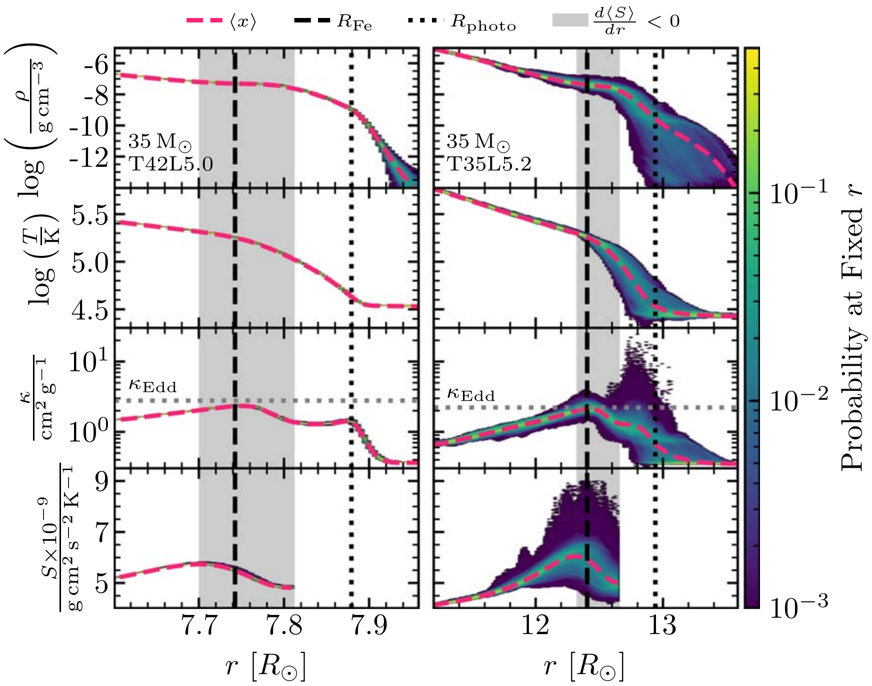

Figure 2. Profiles of density, temperature, opacity, and entropy (top to bottom, respectively) from a single temporal snapshot of T42L5.0 (left) and T35L5.2 (right). The pink dashed lines show the radial profile generated from a volume-weighted shell average and the color shows the probability that each quantity has the specified value at that radius. The sum of the color along vertical lines in each panel is 1. The vertical dashed black line shows the location of the iron-opacity peak and the dotted black line represents the photosphere (where $\langle\tau\rangle = 1$). The gray shaded region denotes where the average entropy gradient is negative. In the κ panel, the horizontal line represents the opacity above which the model is super-Eddington.

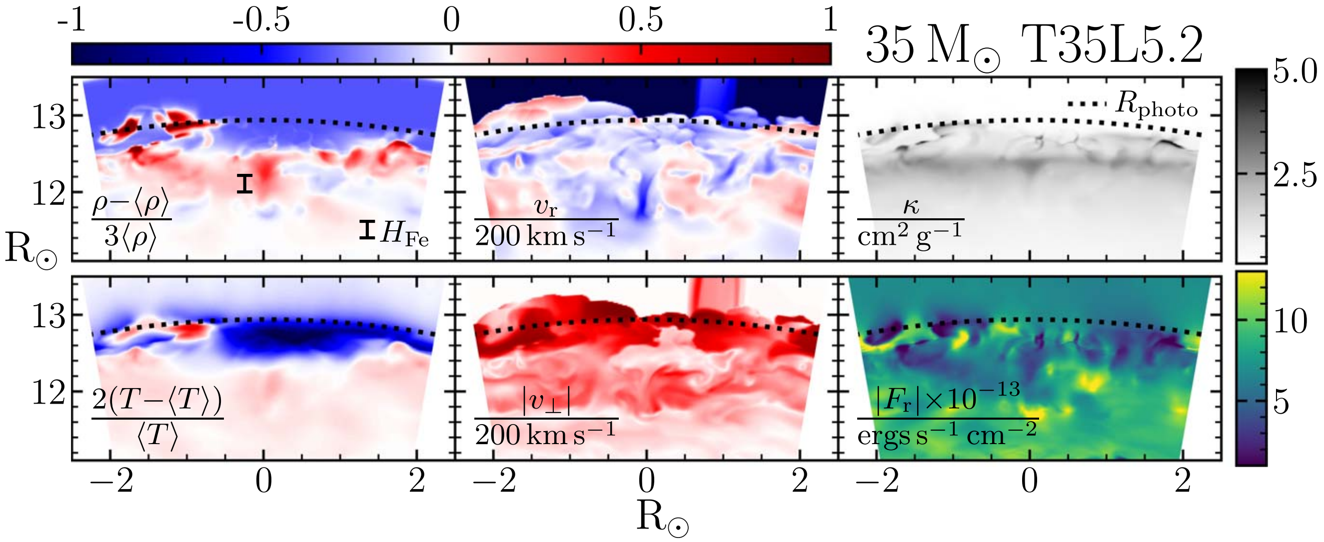

Figure 3. Slices of overdensity, radial velocity, opacity, diffusive radiative flux, tangential velocity magnitude, and overtemperature (clockwise from upper left respectively) though a θ–r plane of a single temporal snapshot from T35L5.2. The black dotted line shows the photosphere for the entire snapshot and the scale height at the iron-opacity peak, $H_{\rm Fe}$, is denoted by the scale bar.

in the FeCZ carries ≈12% of the total flux and the motion of the convective plumes cause significant variations at higher altitudes. As seen in red supergiant models (Goldberg et al. 2021), we find that overdensities propagate upward due to radiative accelerations, but here are associated with the He opacity peak near the surface. Despite the luminosity being larger than the local Eddington luminosity near the Fe and He opacity peaks, the radially averaged density profile does not have any inversions that plague 1D models.

Shell-averaged radial profiles of T35L5.2 are more compact than the initial 1D MESA model due to reduced radiation support caused by correlations between $F_{\rm r}$, ρ, and κ as discussed in Schultz et al. (2020). These correlations are visible in Figure 3 which displays a θ–r plane slice of a snapshot of T35L5.2. This shows that ρ and κ are correlated while both being inversely correlated with $F_{\rm r}$ leading to a reduced radiative pressure gradient $\nabla P_{\rm r}$. Not enough turbulence was generated in T42L5.0 for the correlations to lead to substantial reductions in $\nabla P_{\rm r}$, however the correlations are still present just outside the photosphere.

Figure 3 also shows the structure of the opacity, density, and both radial and tangential velocity fields, $v_{\rm r}$ and $v_\perp$, respectively.

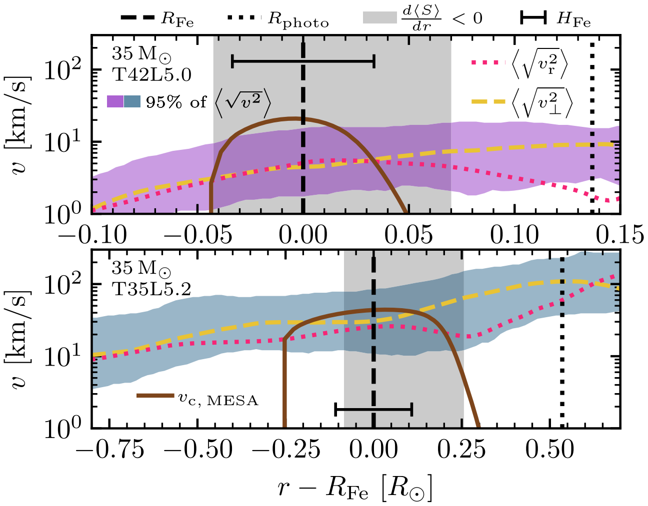

Figure 4. Velocity profiles for single temporal snapshots of T42L5.0 (top) and T35L5.2 (bottom) vs. radius relative to the location of the iron-opacity peak. The colored shaded regions denote the 95% probability interval of the rms velocities at each radius. Dashed gold and dotted red lines are the volume-weighted average rms tangential and radial velocities, respectively. The solid brown line denotes the convective velocity profile from analogous 1D MESA models. The black scale bar shows the extent of the scale height at the iron-opacity peak. Vertical black lines and gray shaded regions are the same as Figure 2.

The Fe opacity peak can be seen as the gray band-like structure at $r \approx 12.7\,R_\odot$ and the dark clumps near the photosphere are peaks from the He opacity. These opaque regions are associated with dense clumps launched from convective plumes, which are as large as the scale height at the iron-opacity peak, $H_{\rm Fe}$. The velocity field is significant throughout the near-surface region, with $v_{\rm r}$ and $v_\perp$ comparable below and at the FeCZ, but $v_\perp$ dominates by a factor of a few at and above the photosphere. As most of the plumes turn around at the photosphere, the radial velocity decreases and the tangential velocity increases slightly as plumes spread out and begin to fall back into the star.

3. Comparisons to Observations

We now compare the surface velocities and photometric variability from the simulations with observations and 1D models.

3.1. Near-surface Convection and Surface Velocities

Figure 4 shows the spread of rms velocities throughout our models as well as typical values for the rms tangential and radial velocities, $\langle\sqrt{v_\perp^2}\rangle$ and $\langle\sqrt{v_{\rm r}^2}\rangle$, respectively. The rms velocities from the 3D RHD models persist well outside the typically defined FeCZ in 1D models, with both significant undershooting and strong velocity fields at the photosphere. The velocity profiles from the MESA models, shown by the brown line in Figure 4, do not extend outside the region where $\frac{dS_{\rm MESA}}{dr} < 0$ though the magnitude of the velocities in these regions are comparable.

Further, our models predict there is no convectively quiet zone between the FeCZ and the photosphere. These convective motions, though carrying minimal flux, create a turbulent region spanning the outer ≈7% of the stellar radial extent, propagating to the photosphere where we see typical surface velocities of $9.3\,{\rm km\,s^{-1}}$ and $123.6\,{\rm km\,s^{-1}}$ in T42L5.0 and T35L5.2, respectively. The three stars similar to T35L5.2 do not have reported macroturbulence velocities, however, the full sample of OB stars have $10 \leqslant v_{\rm macro} \leqslant 120\,{\rm km\,s^{-1}}$ (Burssens et al. 2020). This agreement is striking considering our models are ab initio and are persistent in both our lower resolution models.

Additionally, our models appear to be dominated by tangential velocities at the photosphere, with $\langle\sqrt{v_\perp^2}\rangle / \langle\sqrt{v_{\rm r}^2}\rangle \sim 2$–10. This anisotropy agrees with the recent observational work which determined that radial-tangential fits match observed macroturbulent broadening better than an isotropic Gaussian fit (Simón-Díaz et al. 2010, 2014, 2017) though the extremity of the ratio of the tangential and radial components is debated. Models of IGW propagation predict drastically more tangential motion compared to radial (Aerts et al. 2009), whereas this work and others predict surface disturbances from the FeCZ produce more isotropic velocity fields (Jiang et al. 2015, 2018). Determining anisotropies in surface velocities is therefore vital to understanding whether surface velocities are dominated by IGWs or near-surface convection and more models with direct observational comparisons are needed to verify either hypothesis.

With this agreement, our models strongly support the hypothesis that surface velocities, both macro- and microturbulence, are affected by near-surface convection regions in OB stars with $M \gtrsim 35\,M_\odot$. Additionally, the local velocity fields near the photosphere of our simulations are changing on subhour timescales. How this might manifest in time variability associated with spectral lines has yet to be explored, but it conveys the value of time resolved spectroscopy at ∼10 minutes cadence.

3.2. Stochastic Low-frequency Variability

TESS is revealing that OB stars have ubiquitous SLFV. Specifically, the $\log g$ and $T_{\rm eff}$ of T35L5.2 closely match three O stars (HD41997, HD74920, HD326331) observed by TESS (yellow points outlined in blue in Figure 1). Unfortunately, no observed stars lie near T42L5.0 in the sHRD so a direct comparison can only be carried out for T35L5.2.

Integrated luminosity from model T35L5.2 as a function of time after the FeCZ had safely reached thermal equilibrium is shown in the top panel of Figure 5. To quantify the temporal variability, a first-order polynomial was fit, subtracted, and divided from the model lightcurve to remove the long timescale decrease in luminosity associated with the lack of thermal equilibrium at the base of the model and calculate $\delta L/L$. Utilizing the Python code framework `SciPy` (Virtanen et al. 2020), a Lomb–Scargle periodogram (Lomb 1976; Scargle 1982; Townsend 2010) was calculated from the $\delta L/L$ model lightcurve and the resulting power spectrum, normalized by the low-frequency power, α_0^2, is shown by the solid blue line in the middle panel of Figure 5. Several peaks between $\nu = 2.5$–$7\,{\rm day^{-1}}$ contain nearly an order of magnitude more power than any other frequency in the power spectrum. This is further quantified in the bottom panel of Figure 5, which shows the normalized cumulative power spectrum as the solid blue line contains 4 cliffs that account for 75% of the total power. Our analysis of T35L5.2, T45L5.0, and the lower resolution models showed these quasiperiodic oscillations are caused by convection-driven radial and nonradial pulsations with frequencies and magnitudes that depend on the size of the simulation domain. Properties of these peaks cannot be reliably determined by our simulations.

Aside from the prominent quasiperiodic frequency peaks, SLFV is apparent in T35L5.2. Because the peaks are artifacts

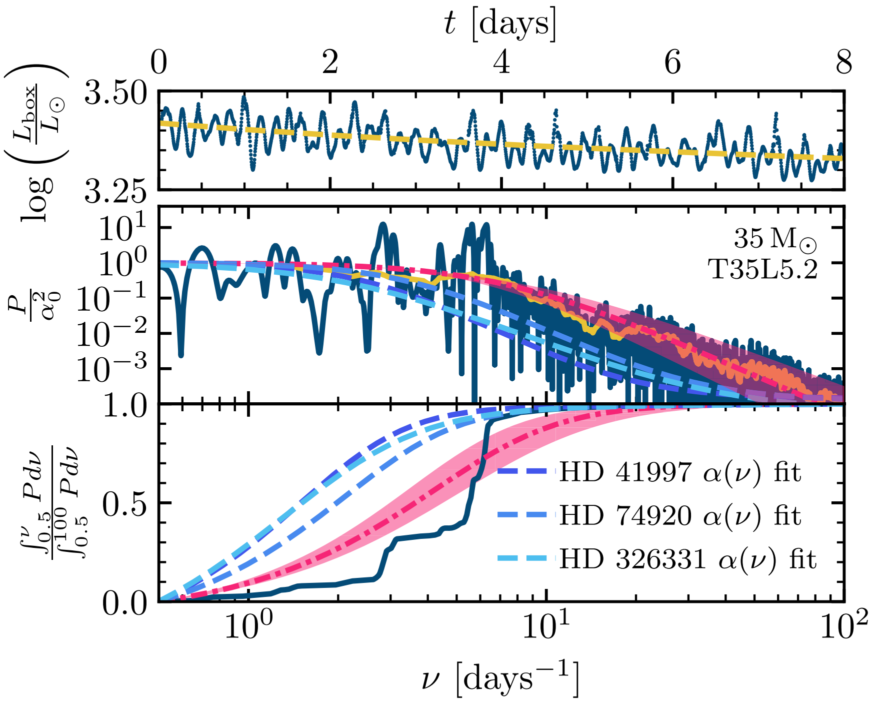

Figure 5. Top: lightcurve of the T35L5.2 model (dark blue points) for 8 days after the model has reached a steady-state equilibrium in the outer regions. The gold dashed line is a first-order polynomial fit of the lightcurve used to zero-mean the lightcurve before taking the power spectrum. Middle: power spectrum of the lightcurve from the top panel (solid dark blue line) compared to the normalized SLF fit, $\alpha(\nu)$, from observed OB stars calculated by Bowman et al. (2020; dashed blue lines of different shades). The colors of the dashed lines match the outlines of the observed locations in Figure 1. The solid gold line shows the result of removing the periodic signals and linearly smoothing the power spectrum. The pink dotted–dashed line denotes the $\alpha(\nu)$ fit from T35L5.2 and the pink shaded region shows the 95% confidence interval. Bottom: cumulative power spectrum of all normalized power spectra on the middle panel normalize to be zero at the left limit ($\nu = 0.5$ day^{-1}) and one at the right edge.

of our simulation domain, they are removed before a fit to the SLFV is carried out. Instead of using the sophisticated prewhitening technique used by Bowman et al. (2019a, 2019b) and others, the peak values were reduced to the mean of the neighboring frequency bins in the power spectrum. Then a simple moving average was used to smooth out the noise in the power spectrum, the result of which is represented by the solid gold line in the middle panel of Figure 5.

Following Bowman et al. (2020), we used a Bayesian Markov Chain Monte Carlo framework with the Python code `emcee` (Foreman-Mackey et al. 2013) to fit the amplitude of the modified power spectrum to $\alpha(\nu) = \alpha_0/(1 + (\nu/\nu_{\rm char})^\gamma) + C_{\rm W}$, where $\nu_{\rm char}$ is a characteristic frequency of the knee in the SLFV, γ sets the slope of the exponential decay, and $C_{\rm W}$ sets the amplitude of the white noise floor. As our model does not have a white noise floor, $C_{\rm W}$ was set to 0 for our fitting. The resulting fit, shown by the pink dotted–dashed line with the 95% confidence intervals shown by the pink shaded region in Figure 5, found $\alpha_0 = 0.0023 \pm 0.0005$ in $\delta L/L$, $\nu_{\rm char} = 7.2 \pm 0.6$ day^{-1} and $\gamma = 1.9 \pm 0.2$ to be the optimal parameters.

The calculated values of α_0, $\nu_{\rm char}$, and γ from the lower resolution model with the same simulation domain agree well with T35L5.2 ($\alpha_0 = 0.0025 \pm 0.0004$ in $\delta L/L$, $\nu_{\rm char} = 7.7 \pm 0.5$ day^{-1} and $\gamma = 1.9 \pm 0.2$). The model with a smaller simulation domain only captures the dynamics of a few plumes causing reduced variability ($\alpha_0 = 0.0016 \pm 0.0005$) and stronger QPOs at different frequencies than T35L5.2. The fit value of $\nu_{\rm char} = 9.5 \pm 0.8$ day^{-1} in the smaller domain model may be affected by the tail of a QPO at 10 day^{-1} that our simple prewhitening prescription cannot sufficiently remove. The plume structure does not appear to affect the power-law slope as the fit value of $\gamma = 1.9 \pm 0.2$ agrees with T35L5.2.

Fits for three comparison stars done by Bowman et al. (2020) are shown by the dashed blue lines in the middle and bottom panels of Figure 5. In an attempt to extrapolate our small simulation domains to cover half a stellar surface, we assume the stellar surface is simply a conglomerate of our models arranged in an uncorrelated manner, we would expect α_0 to be reduced by up to a factor of $\sqrt{n}$, with $n \approx 50$ being the number of models needed to cover the surface, while $\nu_{\rm char}$ and γ would be unaffected. Using this assumption, we predict $\alpha_0 \approx 0.033\%$–0.2% variations in $\delta L/L$, agreeing with observed values (0.03%–0.1% variations). Unfortunately, we cannot check the $\sqrt{n}$ extrapolation by comparing the α_0 of narrower box simulation and T35L5.2. The small number of plumes in the smaller domain model interact and cause the assumption of uncorrelated dynamics to break down. To adequately confirm the $\sqrt{n}$ characterization, a simulation domain larger than that of T35L5.2 would need to be conducted, which is beyond the scope of this work.

Additionally, the γ value of the model's SLFV fit agrees well with the observed values of 1.7–2.3. However, the characteristic frequency of our model's power spectral fit, which is consistent with the thermal timescale of the iron-opacity peak region (≈4 hr), is different than the 2.2–3.7 day^{-1} observed in similar stars. Though we have no explanation for this quantitative discrepancy in the exact power spectrum, we remain optimistic that 3D RHD models of main-sequence O stars exhibit SLFV originating from the FeCZ.

The power spectrum of the ZAMS model, T42L5.0, is dominated by a quasiperiodic oscillation driven from a fundamental radial pulsation at $\nu \approx 18$ day^{-1} but still shows the SLFV knee with a smaller amplitude of variability compared to T35L5.2. However, when using the same technique as described above to fit $\alpha(\nu)$ for T42L5.0 we find our prediction of $\alpha_0 \approx 3 \times 10^{-6}$, $\gamma = 3.5 \pm 0.2$, and $\nu_{\rm char} = 1.2 \pm 0.05\,{\rm day}^{-1}$ to be potentially consistent with those of similar hot OB star observations (i.e., HD110360 and HD37041).

4. Conclusion and Future Work

Our two new 3D RHD models show extended FeCZs and contain significant photospheric velocities comparable to those observed in OB stars. Vigorous, trans-sonic, turbulent convection develops in the middle main-sequence model (T35L5.2) causing large variations in ρ and exhibiting a He opacity peak near the surface. There is no quiet region throughout the outer part of the envelope with surface velocities of $\approx$100 km s^{-1}, matching observed macroturbulent velocities as well as showing a slight anisotropy in directionality, with a preference toward tangential versus radial velocities. Lightcurves from both models show prominent SLFV which agrees in amplitude with observed OB stars, but with more power at higher frequencies than observed. These results were consistent with lower resolution and lower spatial domain models providing evidence that our models are adequately resolved.

Inspired by the realization of SLFV in our 3D RHD models, we plan to investigate if stars in other parts of the sHRD with different stellar parameters generate SLFV via near-surface convection zones. Lower mass stars ($M \sim 10\,M_\odot$) are substantially less Eddington limited, with weaker turbulent convection near the surface giving rise to a debate about the origin of their SLFV. The amplitude of the SLFV observed by TESS for these lower mass stars is significantly smaller (Bowman et al. 2020), which could be explained by the weaker effects of the opacity peaks. SLFV is also present in recent observations of the SMC and LMC (e.g., Kourniotis et al. 2014; Bowman et al. 2019b; Dorn-Wallenstein et al. 2020) and we plan to investigate how metallicity impacts the observed variability with future models.

Nearly all the OB stars with SLFV have substantial measured surface rotation velocities (Bowman et al. 2019a, 2019b; Burssens et al. 2020). However, as the inferred rotation periods ($\sim$days) are typically much longer than the eddy turnover times at the opacity peaks ($\sim$1 hr), we are comfortable with our current exploration neglecting rotational effects. Some of the observed OB stars with SLFV are known to have strong magnetic fields (up to $\approx$10 kG) with recent work highlighting that strong fields can potentially alter surface dynamics (Sundqvist et al. 2013; MacDonald & Petit 2019; Jermyn & Cantiello 2020; Cantiello et al. 2021). Although `Athena++` has the capabilities to include magneto-hydrodynamics (see Jiang et al. 2017), most observed stars with SLFV have fields $<$10 kG, so we do not see an immediate cause to investigate magnetic field effects.

We thank May G. Pedersen and Benny Tsang for many helpful conversations and comments. We also thank the referee for comments that clarified aspects of the paper. This research was supported in part by the NASA ATP grant ATP-80NSSC18K0560 and by the National Science Foundation through grant PHY 17-48958 at the KITP. Resources supporting this work were also provided by the NASA High-End Computing (HEC) program through the NASA Advanced Supercomputing (NAS) Division at Ames Research Center. We acknowledge support from the Center for Scientific Computing from the CNSI, MRL: an NSF MRSEC (DMR-1720256) and NSF CNS-1725797. The Flatiron Institute is supported by the Simons Foundation.

ORCID iDs

William C. Schultz https://orcid.org/0000-0003-1796-9849
Lars Bildsten https://orcid.org/0000-0001-8038-6836
Yan-Fei Jiang (姜燕飞) https://orcid.org/0000-0002-2624-3399

References

Aerts, C., Puls, J., Godart, M., & Dupret, M. A. 2009, A&A, 508, 409
Aerts, C., & Rogers, T. M. 2015, ApJL, 806, L33
Bowman, D. M. 2020, FrASS, 7, 70
Bowman, D. M., Aerts, C., Johnston, C., et al. 2019a, A&A, 621, A135
Bowman, D. M., Burssens, S., Pedersen, M. G., et al. 2019b, NatAs, 3, 760
Bowman, D. M., Burssens, S., Simón-Díaz, S., et al. 2020, A&A, 640, A36
Burssens, S., Simón-Díaz, S., Bowman, D. M., et al. 2020, A&A, 639, A81
Cantiello, M., & Braithwaite, J. 2019, ApJ, 883, 106
Cantiello, M., Langer, N., Brott, I., et al. 2009, A&A, 499, 279
Cantiello, M., Lecoanet, D., Jermyn, A. S., & Grassitelli, L. 2021, ApJ, 915, 112
Couston, L.-A., Lecoanet, D., Favier, B., & Le Bars, M. 2018, JFM, 854, R3
Cox, J. P., & Giuli, R. T. 1968, Principles of Stellar Structure (New York: Gordon and Breach)
David-Uraz, A., Owocki, S. P., Wade, G. A., Sundqvist, J. O., & Kee, N. D. 2017, MNRAS, 470, 3672
Dorn-Wallenstein, T. Z., Levesque, E. M., Neugent, K. F., et al. 2020, ApJ, 902, 24
Foreman-Mackey, D., Hogg, D. W., Lang, D., & Goodman, J. 2013, PASP, 125, 306
Goldberg, J. A., Jiang, Y.-F., & Bildsten, L. 2021, arXiv:2110.03261
Goldreich, P., & Kumar, P. 1990, ApJ, 363, 694
Iglesias, C. A., & Rogers, F. J. 1996, ApJ, 464, 943
Jermyn, A. S., & Cantiello, M. 2020, ApJ, 900, 113
Jiang, Y.-F. 2021, ApJS, 253, 49
Jiang, Y.-F., Cantiello, M., Bildsten, L., et al. 2018, Natur, 561, 498
Jiang, Y.-F., Cantiello, M., Bildsten, L., Quataert, E., & Blaes, O. 2015, ApJ, 813, 74
Jiang, Y.-F., Cantiello, M., Bildsten, L., Quataert, E., & Blaes, O. 2017, ApJ, 843, 68
Joss, P. C., Salpeter, E. E., & Ostriker, J. P. 1973, ApJ, 181, 429
Kourniotis, M., Bonanos, A. Z., Soszyński, I., et al. 2014, A&A, 562, A125
Krtička, J., & Feldmeier, A. 2018, A&A, 617, A121
Krtička, J., & Feldmeier, A. 2021, A&A, 648, A79
Lecoanet, D., Cantiello, M., Quataert, E., et al. 2019, ApJL, 886, L15
Lecoanet, D., & Quataert, E. 2013, MNRAS, 430, 2363
Lomb, N. R. 1976, Ap&SS, 39, 447
MacDonald, J., & Petit, V. 2019, MNRAS, 487, 3904
Moffat, A. F. J., Marchenko, S. V., Zhilyaev, B. E., et al. 2008, ApJL, 679, L45
Paxton, B., Bildsten, L., Dotter, A., et al. 2011, ApJS, 192, 3
Paxton, B., Cantiello, M., Arras, P., et al. 2013, ApJS, 208, 4
Paxton, B., Marchant, P., Schwab, J., et al. 2015, ApJS, 220, 15
Paxton, B., Schwab, J., Bauer, E. B., et al. 2018, ApJS, 234, 34
Paxton, B., Smolec, R., Schwab, J., et al. 2019, ApJS, 243, 10
Ricker, G. R., Winn, J. N., Vanderspek, R., et al. 2015, JATIS, 1, 014003
Scargle, J. D. 1982, ApJ, 263, 835
Schultz, W. C., Bildsten, L., & Jiang, Y.-F. 2020, ApJ, 902, 67
Simón-Díaz, S., Aerts, C., Urbaneja, M. A., et al. 2018, A&A, 612, A40
Simón-Díaz, S., Godart, M., Castro, N., et al. 2017, A&A, 597, A22
Simón-Díaz, S., Herrero, A., Sabín-Sanjulián, C., et al. 2014, A&A, 570, L6
Simón-Díaz, S., Herrero, A., Uytterhoeven, K., et al. 2010, ApJL, 720, L174
Stone, J. M., Tomida, K., White, C. J., & Felker, K. G. 2020, ApJS, 249, 4
Sundqvist, J. O., Petit, V., Owocki, S. P., et al. 2013, MNRAS, 433, 2497
Townsend, R. H. D. 2010, ApJS, 191, 247
Virtanen, P., Gommers, R., Oliphant, T. E., et al. 2020, Nat. Methods, 17, 261